Journal of Integrative Neuroscience

J. Integr. Neurosci. **2023**; 22(3): 73
https://doi.org/10.31083/j.jin2203073

Review

Role of Advanced MR Imaging in Diagnosis of Neurological Malignancies: Current Status and Future Perspective

Akram M Eraky[1], Ryan T. Beck[2], Randall W. Treffy[1], Daniel M. Aaronson[1], Hirad Hedayat[1,*]

[1]Department of Neurosurgery, Medical College of Wisconsin, Milwaukee, WI 53226, USA
[2]Department of Radiology, Medical College of Wisconsin, Milwaukee, WI 53226, USA
*Correspondence: Hhedayat@mcw.edu (Hirad Hedayat)
Academic Editor: Gernot Riedel
Submitted: 7 February 2023 Revised: 28 March 2023 Accepted: 30 March 2023 Published: 15 May 2023

Abstract

Lesions of the central nervous system (CNS) can present with numerous and overlapping radiographical and clinical features that make diagnosis difficult based exclusively on history, physical examination, and traditional imaging modalities. Given that there are significant differences in optimal treatment protocols for these various CNS lesions, rapid and non-invasive diagnosis could lead to improved patient care. Recently, various advanced magnetic resonance imaging (MRI) techniques showed promising methods to differentiate between various tumors and lesions that conventional MRI cannot define by comparing their physiologic characteristics, such as vascularity, permeability, oxygenation, and metabolism. These advanced MRI techniques include dynamic susceptibility contrast MRI (DSC), diffusion-weighted imaging (DWI), dynamic contrast-enhanced (DCE) MRI, Golden-Angle Radial Sparse Parallel imaging (GRASP), Blood oxygen level-dependent functional MRI (BOLD fMRI), and arterial spin labeling (ASL) MRI. In this article, a narrative review is used to discuss the current trends in advanced MRI techniques and potential future applications in identifying difficult-to-distinguish CNS lesions. Advanced MRI techniques were found to be promising non-invasive modalities to differentiate between paraganglioma, schwannoma, and meningioma. They are also considered promising methods to differentiate gliomas from lymphoma, post-radiation changes, pseudoprogression, demyelination, and metastasis. Advanced MRI techniques allow clinicians to take advantage of intrinsic biological differences in CNS lesions to better identify the etiology of these lesions, potentially leading to more effective patient care and a decrease in unnecessary invasive procedures. More clinical studies with larger sample sizes should be encouraged to assess the significance of each advanced MRI technique and the specificity and sensitivity of each radiologic parameter.

Keywords: BOLD; fMRI; perfusion-MRI; DWI; ASL; (DCE) MRI; MRI (DSC); paraganglioma; schwannoma; neurofibromatosis type 2 (NF2); meningioma; glioblastoma multiforme (GBM); lymphoma; metastases; glioma; pseudoprogression

1. Introduction

Neurological tumors differ significantly in their microstructure, molecular constructs, common anatomic locations, and classic features on conventional imaging [1]. However, their imaging features and anatomic locations can overlap and are not specific enough for diagnosis [2,3]. For these reasons, a definitive diagnosis can often only be achieved using biopsy for histopathological confirmation, which is invasive and challenging in some locations [1]. Recently, many advanced magnetic resonance imaging (MRI) techniques have been used for tumor differentiation by assessing the internal biological features of different tumors, such as their vascularity, cellularity, oxygenation, and microstructure [4–6]. This provides non-invasive, rapid novel techniques to differentiate between neurologic tumors, guide treatment plans, and avoid unnecessary surgeries.

This article aims to provide a review of the use of advanced MRI techniques in neurologic tumor differentiation and outline advances underlying current evidence. To our knowledge, this is the first review of the potential of advanced MRI techniques in assisting diagnosis of neurologic tumors.

In contrast to conventional MRI, which delineates the anatomical structures and shows gross changes in the structure of the tumor, advanced MRI techniques represent dynamic physiological properties of tissue, which may be helpful in differentiating undiagnosed lesions based on properties including vascularity, cellularity, and metabolism [7–9]. The term advanced MRI techniques is used throughout this article to refer to dynamic contrast-enhanced (DCE) MRI, dynamic susceptibility contrast (DSC) MRI, diffusion-weighted imaging (DWI), arterial spin labeling (ASL) MRI, and blood oxygen level-dependent functional MRI (BOLD fMRI). In Figs. 1,2, we present different MRI images of two cases with different brain lesions including right frontal lobe oligodendroglioma (WHO grade II) and left lateral ventricle cavernous malformation. These two figures demonstrate the main differences between conventional MRI which delineates the anatomical borders of the brain lesions and advanced MRI techniques which demonstrate the internal physiologic features of different tumors, such as their vascularity, cellularity, perfusion, oxygenation, and microstructure.

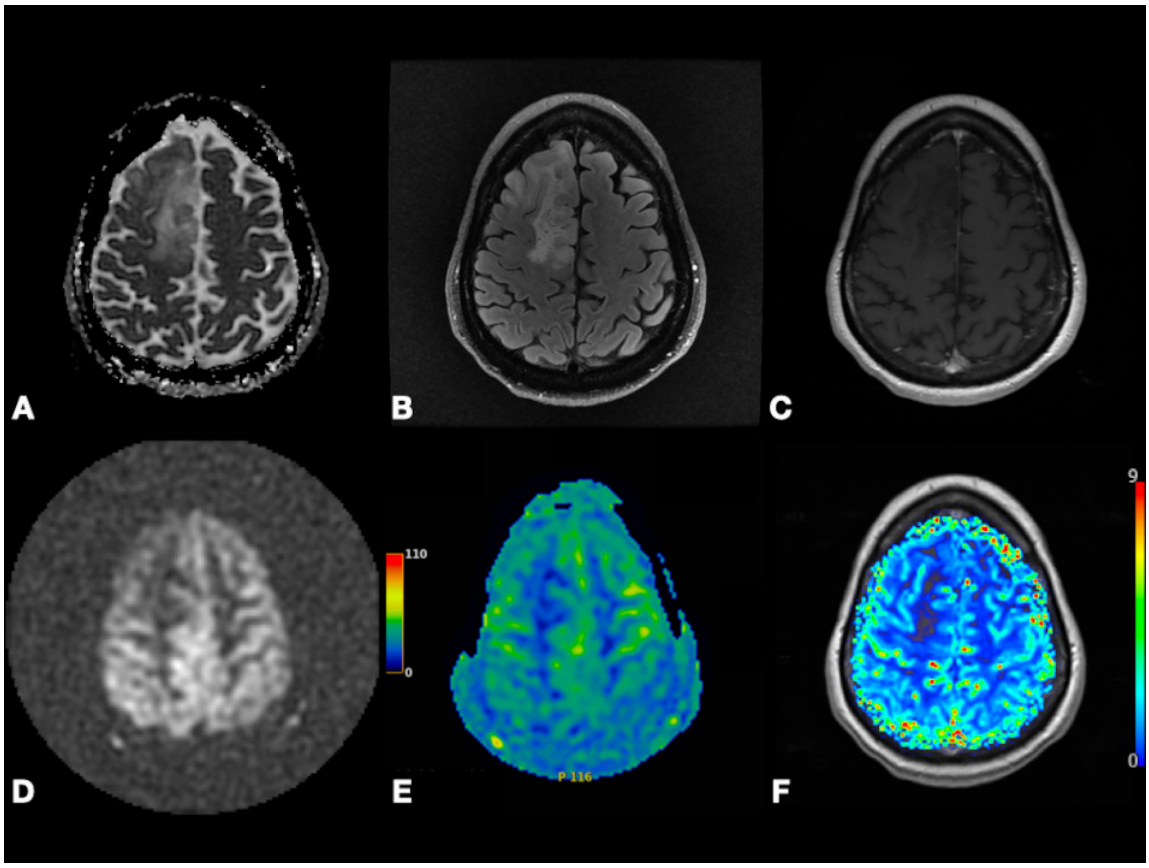

Fig. 1. Right frontal lobe oligodendroglioma (WHO Grade 2). Axial ADC map (A), FLAIR (B), and post-contrast T1-weighted (C) images depicting non-enhancing tumor with T2 prolongation in gray and white matter and increased diffusivity (i.e., shine-through artifact). Axial pcASL source data (D), color-coded CBF map (E) from pcASL data, and color-coded rCBV map (F) from DSC data depicting no hyperperfusion. Abbreviation: ADC, Apparent diffusion coefficient; FLAIR, Fluid attenuated inversion recovery; pcASL, Pseudo-Continuous Arterial Spin Labeling; CBF, cerebral blood flow; rCBV, relative cerebral blood volume; DSC, Dynamic susceptibility contrast MR imaging.

1.1 Perfusion-MRI

Perfusion MRI or perfusion-weighted imaging (PWI) techniques provide information about hemodynamic parameters such as cerebral blood volume, cerebral blood flow, and transit time by following the temporal passage of specific particles through the microvascular bed of the lesion of interest. Perfusion MRI sequences are considered relatively advanced tools that have been used recently for differentiation between various neurological and non-neurological tumors and include 3 main techniques: DCE-MRI, DSC-MRI, and ASL [8,10,11].

In contrast to DCE and DSC techniques that use gadolinium particles as an exogenous tracer, ASL quantifies cerebral blood perfusion by labeling arterial blood water molecules magnetically as endogenous tracers [10,12]. By acquiring a control image before the arrival of the labeled water protons and the subtracted difference between the tagged and control images, ASL visualizes cerebral perfusion with avoidance of cerebral blood flow (CBF) overestimation [13,14].

DSC-MRI relies on the temporal measure of signal changes during the injected paramagnetic gadolinium particles' passage [15,16]. The qualitative nature of DSC results is considered a severe limitation [17]. For obtaining quantitative results, the technique is extended by Rempp *et al*. [18]. Gadolinium particles decrease the signal intensity of T2 images so that the changes in gadolinium concentration can infer three important parameters including cerebral blood flow (CBF), cerebral blood volume (CBV), and the mean transit time (MTT) by applying tracer kinetic theory [19,20]. CBF represents the blood volume passing through a specific region of brain tissue per unit of time, while CBV represents the blood volume that occupies a specific brain region [15]. It is usually termed relative cerebral blood volume (rCBV) as the arterial input function is not measured in most cases [21]. In the case of brain tumors, rCBV is considered the ratio between CBV in the tumor and CBV in the contralateral white matter [22]. MTT equals CBV divided by CBF and represents the average time for a gadolinium particle to pass through the vascular bed of the lesion or region of interest [15].

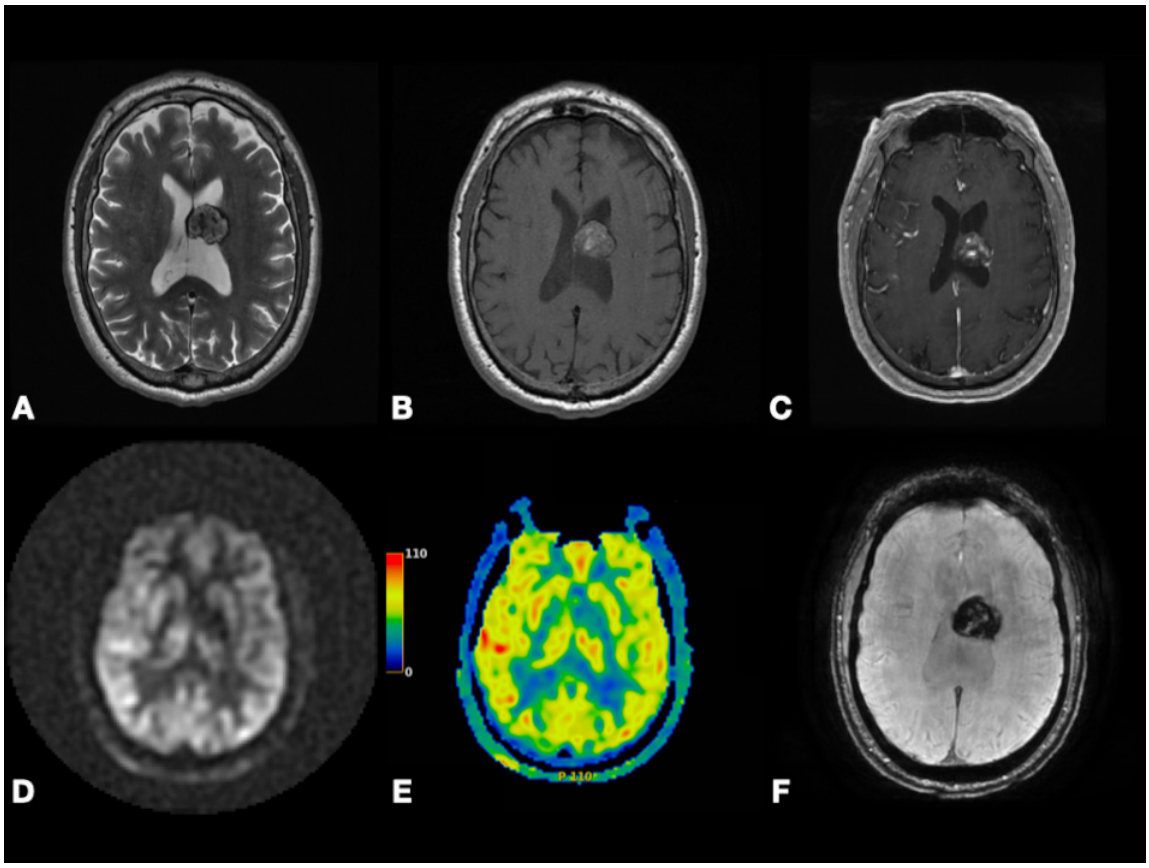

Fig. 2. Left lateral ventricle cavernous malformation. Axial T2-weighted (A), pre- and post-contrast T1-weighted (B,C), and SWI (F) images depicting lesion with heterogenous enhancement, heterogenous predominantly hyperintense signal, peripheral hemosiderin rim, and extensive blooming. Axial pcASL source data (D) and color-coded CBF map (E) depicting no hyperperfusion. Abbreviations: SWI, Susceptibility weighted imaging; pcASL, Pseudo-Continuous Arterial Spin Labeling; CBF, cerebral blood flow.

DCE-MRI quantifies the pharmacokinetics of the injected gadolinium particles as illustrated in Fig. 3 [23]. Gadolinium passage increases the signal intensity of T1, so T1 signal intensity changes before, during, and after administration can indicate permeability and vascularity of the lesion of interest [24,25]. By applying the pharmacokinetic model described by Tofts *et al*. [26], quantitative parameters can be measured like fractional plasma volume (V_p) that indicates tumor vascularity, fractional volume of extracellular space (EES) per unit tissue volume (V_e), forward volume transfer constant between EES and plasma (K_{trans}), efflux rate constant (K_{ep}), and maximum signal-enhancement ratio (SER) [7,9,24–27]. Both V_e and K_{trans} reflect permeability [28]. Also, semi-quantitative parameters can be obtained by using a model-free approach, such as area under the curve (AUC) indicating the relative quantity of contrast agent over time, peak intensity, wash-in rate, wash-out rate, time to peak, and time to onset [7–9,25,28].

High temporal and spatial resolution can be provided by continuous 3D data acquisition through a new DCE technique called Golden-Angle Radial Sparse Parallel (GRASP) MR imaging [29–31]. GRASP has the same qualitative, semiquantitative, and quantitative parameters as DCE. Using DCE and GRASP, there are three types of time-intensity curve (TIC) patterns representing qualitative parameters as illustrated in Fig. 4. TIC type (1) represents rapid wash-in followed by continuous persistent enhancement representing slower wash-in without washout, while TIC type (2) demonstrates rapid wash-in followed by a plateau, and TIC type (3) shows rapid wash-in followed by slow washout [29,30].

1.2 Diffusion-Weighted Imaging (DWI)

DWI depicts the water molecules' diffusion in biological tissues, thus allowing diffusion process mapping [32]. It can reflect cellular membrane integrity and tissue cellularity [27]. DWI should be performed at two or more b values (b-value is a factor reflecting the gradients' time and strength to generate DWI images). Apparent diffusion coefficient (ADC) is a quantitative parameter reflecting water molecules' diffusion ability [33]. It is derived from the gradient of the signal intensity (SI) log between at least two b-values as illustrated in Fig. 5. In the case of presence of factors restricting water diffusion, the ADC value is decreased [9].

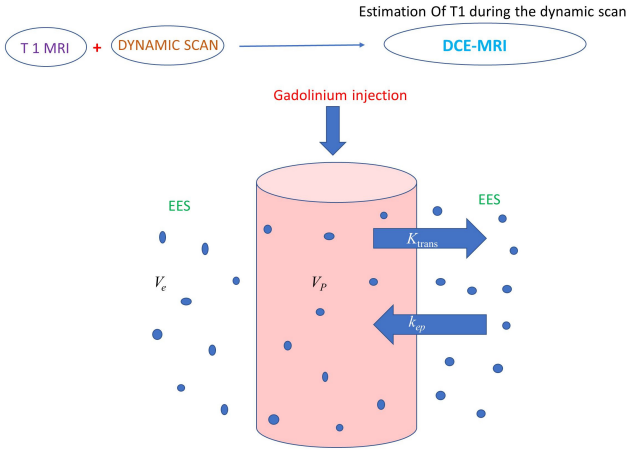

Fig. 3. Illustration showing a two-compartment model (plasma space and extravascular and extracellular space) to calculate gadolinium pharmacokinetic parameters. DCE-MRI involves rapid multiple T1 images before, during, and after gadolinium administration to quantify microvascular permeability. V_p indicates tumor vascularity, while both V_e and K_{trans} reflect permeability. Abbreviations: DCE-MRI, dynamic-contrast enhanced MRI; EES, extravascular extracellular space; V_p, blood plasma volume per unit tissue volume; V_e, EES volume per unit tissue volume; K_{trans}, volume transfer constant from plasma to EES; K_{ep}, rate constant from EES to plasma [$K_{ep} = K_{trans}/V_e$].

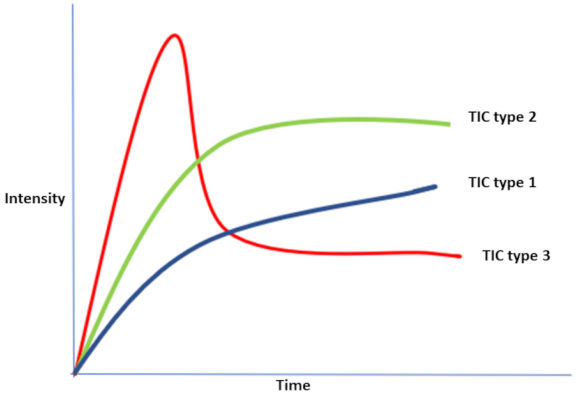

Fig. 4. Illustration showing the three possible types of TIC patterns representing qualitative parameters produced by DCE or GRASP. TIC type (1) represents rapid wash-in followed by continuous persistent enhancement representing slower wash-in without washout, while TIC type (2) demonstrates rapid wash-in followed by a plateau, and TIC type (3) shows rapid wash-in followed by slow washout. Abbreviations: DCE-MRI, dynamic-contrast enhanced MRI; TIC, time intensity curve; GRASP, Golden-Angle Radial Sparse Parallel MR imaging.

1.3 Blood Oxygen Level-Dependent (BOLD) Functional MR Imaging

BOLD-MRI is a non-invasive, widespread, low-cost MRI technique demonstrating the temporal regional

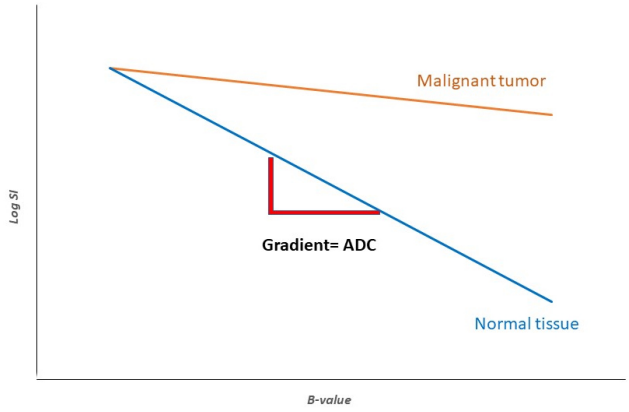

Fig. 5. Illustration showing ADC, a quantitative parameter reflecting water molecules' diffusion ability using DWI. The ADC is derived from the gradient of the MRI signal intensity and at least two b-values. It is influenced by cellular membrane integrity and tissue cellularity. In the case of the presence of factors that can restrict water diffusion, such as fluid viscosity and high cellularity, DWI demonstrates higher levels of SI and subsequently, lower levels of ADC. Abbreviations: SI, signal intensity; ADC, apparent diffusion coefficient; DWI, diffusion-weighted MRI.

changes in brain metabolism. It has commonly been used in cognitive neuroscience, psychiatry, and psychology research [34–37]. Increased metabolism in a specific region in the brain following increased activity in this area induces production of many chemicals (CO_2, NO, H^+) that cause vasodilatation and subsequently increase blood flow and restore O_2 level. This explains why neural stimulation results in accumulation of deoxygenated hemoglobin followed rapidly by a decrease in deoxygenated hemoglobin, and an increase in blood flow [38,39]. BOLD fMRI demonstrates the changes in the magnetic field surrounding red blood cells (RBCs) which depend on the oxygen status [40]. Cerebrovascular reactivity (CVR) is a quantitative parameter representing the cerebral blood vessels' ability to constrict and dilate in response to vasoactive challenges and can be measured by BOLD-fMRI [41].

1.4 Clinical Features and Conventional MRI Characteristics of the Extra-Axial Lesions (Paraganglioma (PG), Schwannoma (SC), and Meningioma (MG))

Paragangliomas (PGs) are rare, slowly growing neuroendocrine tumors arising from neural crest cells that are present in any autonomic ganglia with the carotid body, middle ear, and jugular foramen as the most common sites [42–44]. Carotid body and cervical sympathetic tumors present with a painless neck mass, and also possibly Horner's syndrome. Jugulotympanic PG, also known as glomus tympanicum and glomus jugulare, can present with hearing loss, tinnitus, and compression on the jugu-

lar foramen contents including the glossopharyngeal nerve, vagus nerve, and accessory nerve [45,46]. In a few cases of PGs, there is catecholamine secretion that can cause hypertension, palpitations, tachycardia, and headache, although all PGs can theoretically secrete catecholamines [47]. On MRI, PGs are visualized as heterogeneously enhancing tumors with salt and pepper appearance and with necrotic or cystic changes [48].

Combination of avid heterogenous enhancement, markedly hyperintense T2-weighted signal with scattered flow voids (salt and pepper appearance), and affecting specific locations including cochlear promontory in middle ear cavity, jugular fossa, and carotid bifurcation favors PG [45–48]. Splaying of carotid bifurcation favors glomus caroticum (carotid body tumor). However, anterior displacement of carotid bifurcation can be seen with glomus vagale or schwannoma (SC) [45–48].

Meningiomas (MGs) are the most common extra-axial brain tumors. They arise from the arachnoid cells and are more common in middle-aged women [49]. Their clinical picture varies according to the compression effect on different locations. The most commonly reported symptom is headache [50–52]. Their most common location is parasagittal and parafalcine areas, followed by convexity, tuberculum sellae, sphenoid ridge, and olfactory groove, respectively [53].

MGs show isointensity to hypointensity on T1, hyperintensity on T2, and post-contrast enhancement. Rarely, it can show cystic changes and internal hemorrhage. Calcifications may also be seen inside the tumor [50,51,54,55]. The cerebrospinal fluid (CSF) cleft sign surrounding extra-axial tumors like MGs, PGs, and SCs is hypointense on T1 because of the CSF accumulation between the lesion and the brain parenchyma, and the blood vessels trapped between the tumor and the brain [50,55,56]. This sign is not specific and can be also found in many other lesions, such as glioma, metastasis (MT), and lymphoma [57–59]. Dural tail on MRI, hyperostosis and dilatation of a paranasal sinus (pneumosinus dilatans) favor MG. MGs are infrequently calcified. Also, bone erosion, invasion, and/or remodeling may be seen with MGs [50–59].

SCs are benign tumors originating from Schwann cells wrapping the nerve sheath. They are considered the second most common extra-axial brain tumor after MGs. Theoretically, SCs can originate from any peripheral and cranial nerve except the optic nerve as it is myelinated by oligodendrocytes, not Schwann cells. Vestibular and trigeminal nerves are the most affected cranial nerves respectively [50,60–65].

Vestibular SCs can grow initially inside the internal auditory canal and then extend into the cerebellopontine angle; it is characterized by absence of CSF signal in the internal auditory canal on MRI imaging. SCs show isointensity to hypointensity on T1, hyperintensity on T2, and post-contrast enhancement. It can show heterogeneous post-contrast enhancement and signal intensity which is suggestive of cystic changes and internal hemorrhage [50,66,67]. The main differential diagnosis of SC in the cerebellopontine angle is MG. The common differences between MG and SC on conventional MRI are summarized in Table 1 [50,66,67]. SCs occupying the foramen magnum usually originate from the glossopharyngeal nerve (CN IX) [50]. Additionally, SCs located in the carotid sheath can only originate from the vagus nerve (CN X) [50]. At both locations, it is difficult to differentiate between SCs versus PGs. Combination of location along an expected course of a cranial nerve and widening or remodeling of adjacent bones, such as porus acousticus of internal auditory canal (IAC) and foramen oval, favors SCs [50,66,67].

2. Role of Advanced MRI Techniques in Differentiating between Paraganglioma (PG) and Schwannoma (SC)

Although on MRI, PGs are visualized as heterogeneously enhancing tumors with salt and pepper appearance with necrotic or cystic changes, SCs can share similar features [48,68,69]. Subsequently, PGs can be misdiagnosed and cause unwanted surprises during and after surgery. The final diagnosis usually relies on their histopathologic features, although the risk of excessive hemorrhage and adrenergic crisis associated with biopsy of highly vascularized PGs and the risk of injury to neurovascular structures in the jugular foramen and carotid sheath make biopsy challenging [70,71]. Therefore, finding a rapid, non-invasive, reliable way to differentiate between these two tumors is ideal.

Recently, advanced MRI techniques have been utilized to differentiate between various tumors. Using DSC, Ota *et al.* [72] found a significant increase in normalized rCBV and normalized rCBF in intracranial PGs compared to SCs. On DCE for neck mass imaging, Malla *et al.* [73] found that wash-in rate, wash-out rate, V_p, K_{trans}, and K_{ep} are significantly higher in PGs compared to SCs; while V_e, time to peak, and time to onset are significantly higher in SCs compared to PGs. Additionally, they found that V_p and K_{trans} have the highest diagnostic value [73]. In contrast to Malla *et al.*'s [73] findings, Ota *et al.* [74] found that the only significant parameter to differentiate between PGs and SCs is V_p while both K_{trans} and V_e are insignificant. PGs' hypervascularity can explain the higher V_p, rCBV, and rCBF compared to SCs [72,74].

Using GRASP, Pires *et al.* [75] and Demerath *et al.* [76] found that all PGs showed TIC type 3 (rapid wash-in followed by slow washout) which can be explained by PGs' hypervascularity and arteriovenous shunting [77]. On the other hand, SCs showed TIC type 1 (rapid wash-in followed by continuous slower wash-in without washout) which can be explained by the increased permeability to the EES caused by the small thin-walled blood vessels [75,76,78]. Pires *et al.* [75] found that V_e is significantly higher in SCs because the thin-walled small vessels in SCs increase

Table 1. Conventional MRI characteristics of meningioma (MG) versus schwannoma (SC) in the cerebellopontine angle.

Feature	Meningioma	Schwannoma
Internal auditory canal involvement	Rare	Almost always
Centered around internal auditory canal	No, eccentric	Yes
Hemorrhage	Rare	More common
Cystic/necrotic changes	Rare	More common
Calcifications	Possible	Less common
Dural tail	Frequent	Rare
Bony reaction	Osteolysis or hyperostosis	Rare
Angle made with dura	Obtuse	Acute

permeability, while AUC, peak enhancement, wash-in rate, washout rate, SER, and V_p are significantly higher in PGs compared to SCs due to PGs' hypervascularity.

On DWI, two retrospective studies of intracranial tumors did not find a significant difference in ADCmean between PGs and SCs [72,74]. Only one study showed significantly lower ADCmean values in PGs compared to SCs; this prospective study included only neck masses [73]. The insignificant difference in ADC values in intracranial tumors is likely because SCs have various microstructures like Antoni A and Antoni B histologic patterns [79]. Antoni A areas are cellular and have high mitotic activity, while Antoni B areas are hypocellular and contain deformed blood vessels with hyalinized walls [80]. SCs size may also play a role as cystic changes are more likely to develop in larger SCs and these cystic changes might increase ADC values [74,81]. Based on these studies, ADC values may not be a reliable radiologic biomarker to differentiate between PGs and SCs.

3. Role of Advanced MRI Techniques in Differentiating between Sporadic Vestibular Schwannomas (SCs) and Neurofibromatosis Type 2 Associated Vestibular Schwannomas (NF-2 Related SCs)

A mutation in the neurofibromatosis type 2 (*NF2*) gene on chromosome 22 causes an autosomal dominant multiple-tumor syndrome called *NF2* [82]. It is associated with the development of many nervous system tumors including SCs, MGs, and gliomas [83–86]. Although bilateral SC is considered a characteristic that is nearly diagnostic of *NF2* and affects 95% of NF2 patients, NF2 can present with unilateral SC [87].

Using DSC, Ota *et al.* [72] also found a significant increase in normalized rCBV and normalized rCBF in *NF2*-related SCs compared to sporadic SCs. Using DCE, another study showed that K_{trans} and V_e are significantly higher in *NF2*-associated SCs compared to sporadic SCs [88]. A previous study showed that SC's growth (*NF2*-related SCs typically grow faster than sporadic SCs [89]) can influence permeability, with increased permeability in *NF2*-associated SCs as indicated by high rCBF, rCBV, K_{trans}, and V_e [90].

Using DWI, a significant decrease in mean normalized ADC in *NF2*-related SCs compared to sporadic SCs is observed [72,88]. This may be explained by the features of *NF2*-associated SCs including presence of hypercellular foci, whorl patterns, and lobular patterns, leading to restricted fluid diffusion in *NF2*- associated SCs; these features are not typically seen in sporadic SCs [91,92].

4. Role of Advanced MRI Techniques in Differentiating between Meningioma (MG) versus Schwannoma (SC), and Paraganglioma (PG)

Differential diagnosis of parasellar tumors includes PGs, MGs, and pituitary adenoma. Rarely, PGs can also occupy the parasellar region [2]. On conventional MRI, it is difficult to differentiate between these tumors [2]. Similarly, it is difficult to differentiate between MGs and vestibular SCs in the cerebellopontine angle and internal auditory canal [93]. Advanced MRI techniques show a promising non-invasive rapid modality to differentiate between MGs and SCs or PGs.

Using DCE, Ota *et al.* [74] revealed that V_p is significantly lower in MGs compared to PGs. Additionally, V_e and K_{trans} are significantly higher in MGs compared to PGs indicating that MGs have lower vascularity and higher permeability compared to PGs [74]. Compared to MGs, V_p, and K_{trans} are found to be significantly lower in SCs. This represents higher vascularity and permeability in MGs compared to SCs [74].

On DWI, Pavlisa *et al.* [94] found that ADCmean in SCs is significantly higher than both typical and atypical MGs. However, Ota *et al.* [74] found that there is no significant difference in ADC values between SCs versus MGs, PGs versus MGs, or SCs versus PGs. Thus, more clinical studies containing a large sample size are needed to evaluate the significance of DWI to differentiate between MGs and other extra-axial tumors. In Fig. 6, we present a case of right cerebral convexity atypical MG. The axial ADC map shows reduced diffusivity, while axial Pseudo-Continuous Arterial Spin Labeling (pcASL) source data and grayscale CBF map show marked heterogenous hyperperfusion. This demonstrates that MGs have high permeability and low diffusivity as mentioned in the literature. All of the previously mentioned studies differentiating between PG, SC, and MG

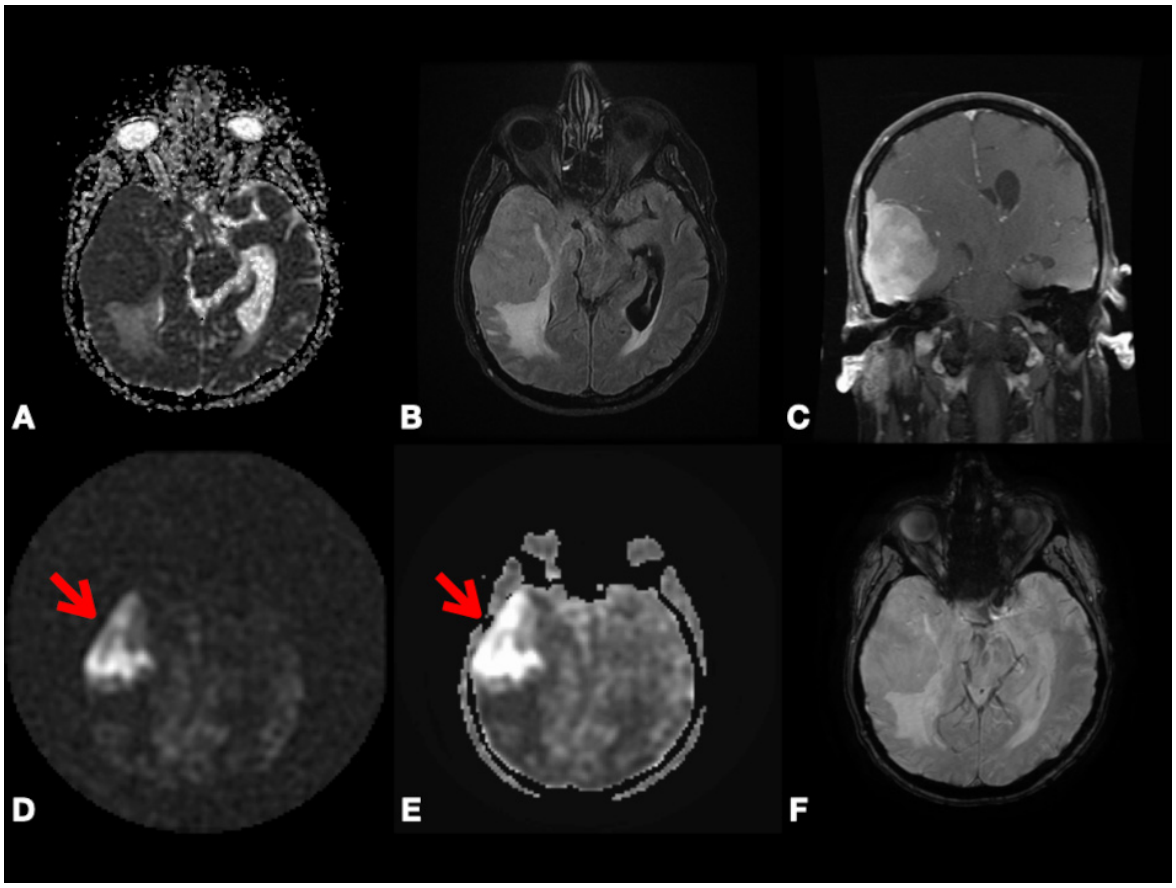

Fig. 6. Right cerebral convexity atypical meningioma (WHO Grade II). Axial ADC map (A), axial FLAIR (B), coronal fat-suppressed post-contrast T1-weighted (C), and axial SWI (F) images depicting large avidly enhancing plaque-like non-calcified mass with dural tail, reduced diffusivity, extensive vasogenic edema and mass effect with uncal herniation and ventricular trapping. Axial pcASL source data (D) and grayscale CBF map (E) depicting marked heterogenous hyperperfusion (red arrows). Abbreviations: ADC, Apparent diffusion coefficient; FLAIR, Fluid attenuated inversion recovery; SWI, Susceptibility weighted imaging; pcASL, Pseudo-Continuous Arterial Spin Labeling; CBF, cerebral blood flow.

using DCE, DSC, GRASP, and DWI are mentioned in Table 2 (Ref. [72–76,88,94]).

5. Role of Advanced MRI Techniques in Gliomas

Anywhere in the central nervous system, glial cells can develop into gliomas, which are considered the most common primary brain tumors in adults [95]. Finding non-invasive biomarkers, such as serum long non-coding RNAs and micro RNAs to diagnose gliomas, differentiate them from post-radiologic changes and MT, and identify glioma grading is a trend now [95]. Advanced MRI techniques are also promising non-invasive modalities to differentiate gliomas from lymphoma, post-radiation changes, pseudo-progression, demyelination, and MT.

5.1 Role of Advanced MRI Techniques in Differentiating Glioma versus Lymphoma

Primary central nervous system lymphoma (PCNSL) is a non-Hodgkin's lymphoma located in the central nervous system including the spinal cord, brain, leptomeninges, and eyes. It presents often as a single brain mass in both immunocompetent and immunocompromised patients [96,97]. No survival benefit is observed after surgical resection, and surgery is associated with higher risks; thus, the role of surgery is limited to biopsy [98,99]. High doses of intravenous methotrexate is an effective treatment. Additionally, corticosteroids can decrease tumor-surrounding edema [100,101]. Periventricular location, hyperdensity on CT, and T2 shortening (hypointense T2-weighted signal) on MRI favor lymphoma. However, on conventional MRI, PCNSL differentiation from high-grade glioma is difficult and sometimes impossible due to its diffuse infiltrative nature and occasional presence of atypical features like necrosis, hemorrhage, or heterogeneous enhancement [102,103]. Given the significant survival benefit with surgical resection of a glioma (compared to no benefit with lymphoma), as well as the desire to start corticosteroids as soon as possible, there would be a substantial benefit to better differentiate the two lesions rapidly and non-invasively [95,101].

Table 2. Characteristics of studies included in our review of differentiating between paraganglioma (PG), schwannoma (SC), and meningioma (MG) using dynamic contrast-enhanced (DCE), dynamic-susceptibility contrast (DSC), Golden- Angle Radial Sparse Parallel (GRASP), and diffusion-weighted (DWI) MRI techniques.

Re.	Year	Study design	Number of patients	Location	Age mean/range	M/F	Histopathology	Type of technique	Significant parameters
[72]	2022	R	41	Intracranial-Infratentorial	7–74	18/23	PG (12)/SC (29)	DSC	nrCBV, nrCBF
[72]	2022	R	29	Intracranial-Infratentorial	N/A	N/A	Sporadic SC (19)/NF2-related SC (10)	DSC, DWI	nrCBV, nrCBF, nADCmean
[73]	2021	P	40	Neck	32.65 +/- 12.36	24/16	PG (33)/SC (15)	DCE, DWI	Wash-in rate, wash-out rate, K_{trans}, K_{ep}, V_p, V_e, time to beak, time to onset, and ADCmean
[74]	2021	R	57	Cerebellopontine angle, jugular foramen	51.2 +/- 17.8	16/41	MG (35)/PG (30) /SC (20)	DCE, DWI	K_{trans}, K_{ep}, V_p, V_e
[88]	2021	R	28	Vestibular	11–67	19/9	Sporadic SC (23)/NF2-related SC (5)	DCE, DWI	K_{trans}, V_e, nADCmean
[94]	2008	P	41	N/A	18–83	19/22	SC (15)/MG (26)	DWI	ADC
[76]	2020	R	11	Head and neck	N/A	N/A	PG (6)/SC (5)	GRASP	TIC
[75]	2021	R	30	Jugular foramen	49.5/26–79	N/A	PG (22)/SC (8)	GRASP	TIC/V_e/V_p/AUC/ peak enhancement/wash-in rate/washout rate/SER

Re., reference; R, retrospective; P, prospective; M, male; F, female; N/A, not applicable; SC, schwannoma; PG, paraganglioma; NF2, neurofibromatosis type 2; DSC, dynamic susceptibility contrast MRI; DWI, diffusion-weighted MRI; nrCBV, normalized relative cerebral blood volume; nrCBF, normalized relative cerebral blood flow; nADCmean, normalized mean apparent diffusion coefficient; MG, meningioma; DCE, dynamic contrast-enhanced; V_p, blood plasma volume per unit tissue volume; V_e, extravascular extracellular volume per unit tissue volume; K_{trans}, volume transfer constant from plasma to extravascular extracellular space; K_{ep}, rate constant from extravascular extracellular space to plasma; ADC, apparent diffusion coefficient; GRASP, Golden-Angle Radial Sparse Parallel MR imaging; TIC, time intensity curve; SER, maximum signal-enhancement ratio.

On DSC, many studies have shown that CBV is significantly lower in PCNSL compared to gliomas [104–109]. Additionally, other studies demonstrate that the maximum rCBV ratio is significantly lower in PCNSL than in gliomas [110,111]. Both corrected CBV ratio and uncorrected CBV ratio are significantly lower in PCNSL [112–114]. Another study demonstrated the ability of CBF to differentiate between PCNSL and gliomas [115]. Using DCE, Kickingereder *et al*. [116] found that median K_{ep} and median K_{trans} are significantly higher in PCNSLs compared to gliomas. Also, Lu *et al*. [117] and Xi *et al*. [118] found that both K_{trans} and V_e are significantly higher in PCNSL compared to glioblastoma multiforme (GBM). Of interest, yet another study indicated that there is no significant difference in V_e between PCNSL and glioma [116].

Many vascular changes causing increased permeability are observed by electron microscopy in PCNSLs, such as thinned endothelial cells, and increased fenestrations between capillary endothelial cells [119]. Higher vascular permeability in PCNSLs caused by blood brain barrier (BBB) disruption can be the cause of increased permeability parameters like K_{ep}, K_{trans}, and V_e. Also, this increased permeability might be a cause of low CBV values in PCNSLs [113]. Another possible cause of lower CBV in PCNSLs compared to gliomas is lack of neovascularization in PCNSLs as they grow surrounding preexisting vessels; thus, their growth pattern is known to be angiocentric, whereas the blood vessels in gliomas are mainly new vessels [120,121].

5.2 Role of Advanced MRI Techniques in Differentiating Gliomas from Demyelinating Lesions

Some demyelinating lesions are exceedingly difficult to differentiate from tumors. Due to BBB disruption in some demyelinating lesions, these lesions can enhance with contrast and can be misdiagnosed as potential malignant lesions [122,123]. Theoretically, advanced MRI techniques can differentiate between demyelinating lesions and gliomas by comparing vascularity and permeability.

Gliomas, especially high-grade ones, are expected to have higher CBV because of their hypercellularity, high metabolism, and neo-angiogenesis [124]. In 2008 Hourani *et al*. [122] demonstrated that rCBV is significantly higher in high-grade gliomas than in demyelinating lesions. However, in 2011 Blasel *et al*. [125] found that some autoimmune demyelinating lesions can share high levels of rCBV like high-grade gliomas, leading to misdiagnosis and affecting the diagnostic accuracy of DSC. In 2017 Hiremath *et al*. [126] found that combining DSC parameters with diffusion tensor metric parameters improved DSC diagnostic accuracy.

5.3 Role of Advanced MRI Techniques in Differentiating Radiation-Induced Necrosis and Pseudoprogression from Glioblastoma (GBM) Recurrence

The most aggressive gliomas are GBM. Their standard treatment includes surgical removal, chemotherapy, and radiotherapy [95]. After completing radiotherapy, enhancing lesions on conventional MRI can be challenging as these changes can represent true progression, radiation-induced pseudoprogression, or radiation necrosis [127–129]. In case of tumor recurrence, reoperation or changing chemotherapy can be necessary. In contrast, radiation-induced pseudoprogression is self-limited and can be treated conservatively with serial imaging [130,131]. Radiation-induced pseudoprogression results from liquefactive necrosis of the injured area, fibrinoid deposition, and vascular hyalinization [130,132]. It is crucial to differentiate between true progression and radiation-induced changes to avoid any unnecessary surgery or biopsy. Based on the fact that GBM is highly vascular and the radiation-induced changes are not, using vascularity and permeability parameters measured by advanced MRI techniques can easily differentiate between them [133,134]. Using DSC, many studies have shown that CBV is significantly higher in GBM compared to pseudoprogression [133–136].

In Fig. 7, we present a case of left temporal lobe GBM (WHO Grade 4) with false-positive perfusion imaging for recurrence. Using DSC, baseline images showed peripheral hyperperfusion. Four months later after the surgery, images showed enhancement and hyperperfusion concerning for recurrence; the patient underwent subsequent resection with no tumor on pathology. This case shows that using color-coded rCBV maps can be misleading as both tumor recurrence and pseudoprogression may show relatively increased perfusion. However, as we discussed in the earlier paragraph, CBV is found to be significantly higher in GBM recurrence compared to pseudoprogression. This highlights the importance of having more studies comparing CBV between pseudoprogression versus recurrence to define a specific CBV value or threshold that can be associated with GBM recurrence. Calculating the specificity and sensitivity of this CBV value is also encouraged. This also highlights the importance of using quantitative parameters, such as tumoral and peritumoral CBV and CBF to compare between GBM and MTs as depending on observing hyperperfusion signals on the color-coded maps is subjective and can be misleading.

Using BOLD fMRI, Muscas *et al*. [137] found that for both newly diagnosed GBM and radiation-induced necrosis lesions, the CVR values are impaired. Moreover, for the radiation-induced pseudoprogression lesions, the mean CVR values were significantly lower than those in the newly diagnosed GBM lesions. This can be explained by GBM's higher vascularity, neo-angiogenesis, and disrupted BBB that leads to loss of regulative capacity and impaired CVR [137–140]. Also, the nonreactive blood ves-

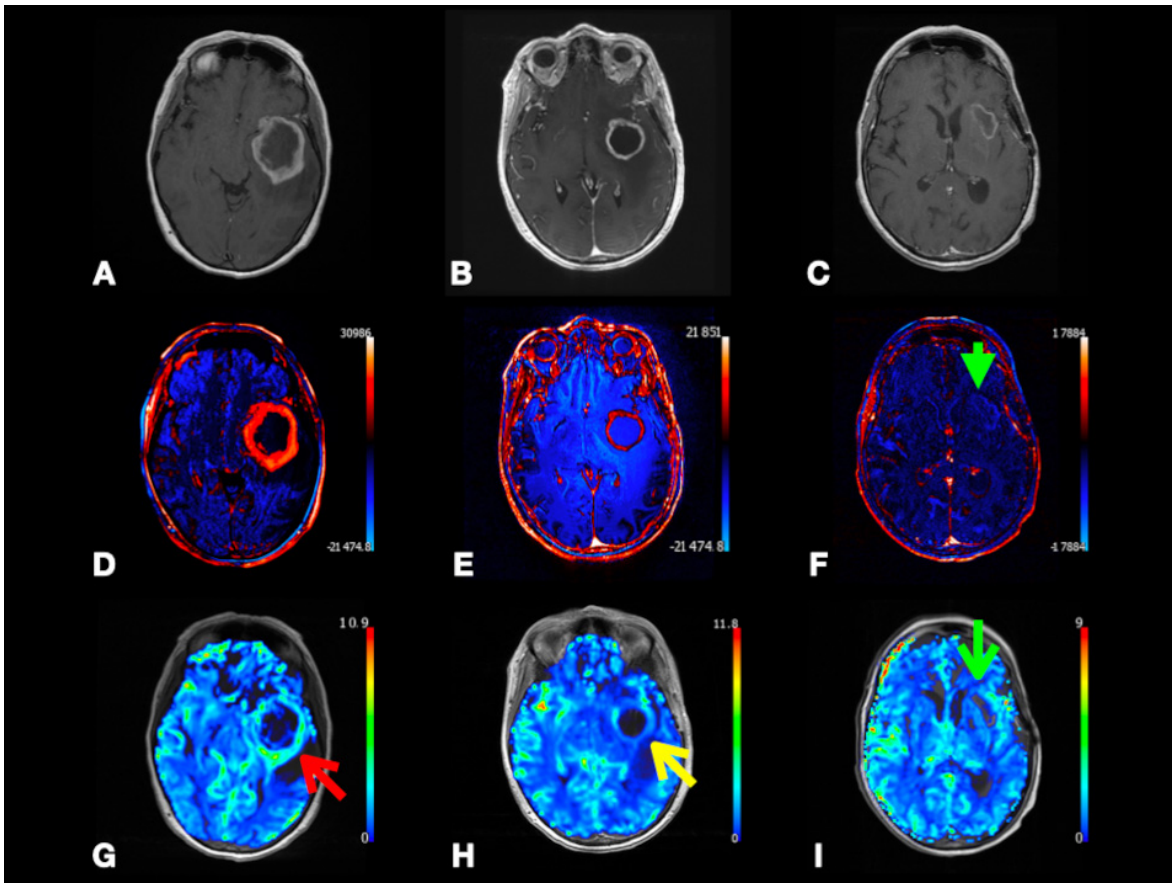

Fig. 7. Left temporal lobe glioblastoma (WHO Grade 4) with false-positive perfusion imaging for recurrence and subsequent treatment-mediated response. Axial post-contrast T1-weighted (A–C), color-coded subtraction maps (D–F), and color-coded rCBV maps (G–I) from DSC data. Baseline images (A,D,G) depicting enhancing mass with central necrosis and peripheral hyperperfusion (red arrow). Images obtained four months later (B,E,H) depicting enhancement and hyperperfusion (yellow arrow) concerning for recurrence; subsequent redo resection with treatment effect and no tumor on pathology. Images obtained eight months later (C,F,I) after temozolomide and Avastin depicting T1 shortening, resolved enhancement (green arrowhead), and resolved hyperperfusion (green arrow) at the superior margin of the expanded resection cavity compatible with treatment response. Abbreviations: rCBV, relative cerebral blood volume; DSC, Dynamic susceptibility contrast MRI.

sels surrounded by necrotic tissues and fibrinoid deposition can cause more impaired CVR [133,136,137]. They also found that for radiation-induced pseudoprogression, there is markedly dramatic CVR improvement in the immediate perilesional areas compared to the perilesional areas in the newly diagnosed GBM that show no significant improvement [137]. GBM's hypermetabolism, neo-angiogenesis, and higher blood flow can cause perilesional vasodilation to bring more blood supply to the lesion. Moreover, the infiltrative and aggressive behavior of GBM can disrupt the existing perilesional blood vessels by the tumor cells surrounding the tumor. Thus, there is no apparent CVR improvement observed in the peritumoral area [137,141,142]. On the other hand, the radiation-induced lesions are focal inflammatory reactions with lower blood flow, so it causes rapid CVR normalization in the perilesional areas [133,135,137].

Of interest, Fierstra *et al.* [143] found that the altered intraoperative BOLD CVR in the peritumoral non-enhancing tissue predicted the exact location of the future tumor recurrence. This can help in achieving optimal tumor resection in the future to decrease the reoperation rate for patients with high-grade gliomas. In contrast to its widespread use in cognitive neuroscience research, very few studies discussed the potential of BOLD fMRI in tumor diagnosis and treatment. More clinical studies are encouraged to examine the BOLD fMRI ability to predict future tumor recurrence and prognosis and differentiate between different tumors.

5.4 Role of Advanced MRI Techniques in Differentiating between Gliomas versus Metastasis (MT)

It is easy to identify MTs from gliomas in the case of presence of systemic MTs or multiple cerebral lesions. However, when the cerebral MTs present as solitary lesions without systemic manifestations, it becomes difficult to dif-

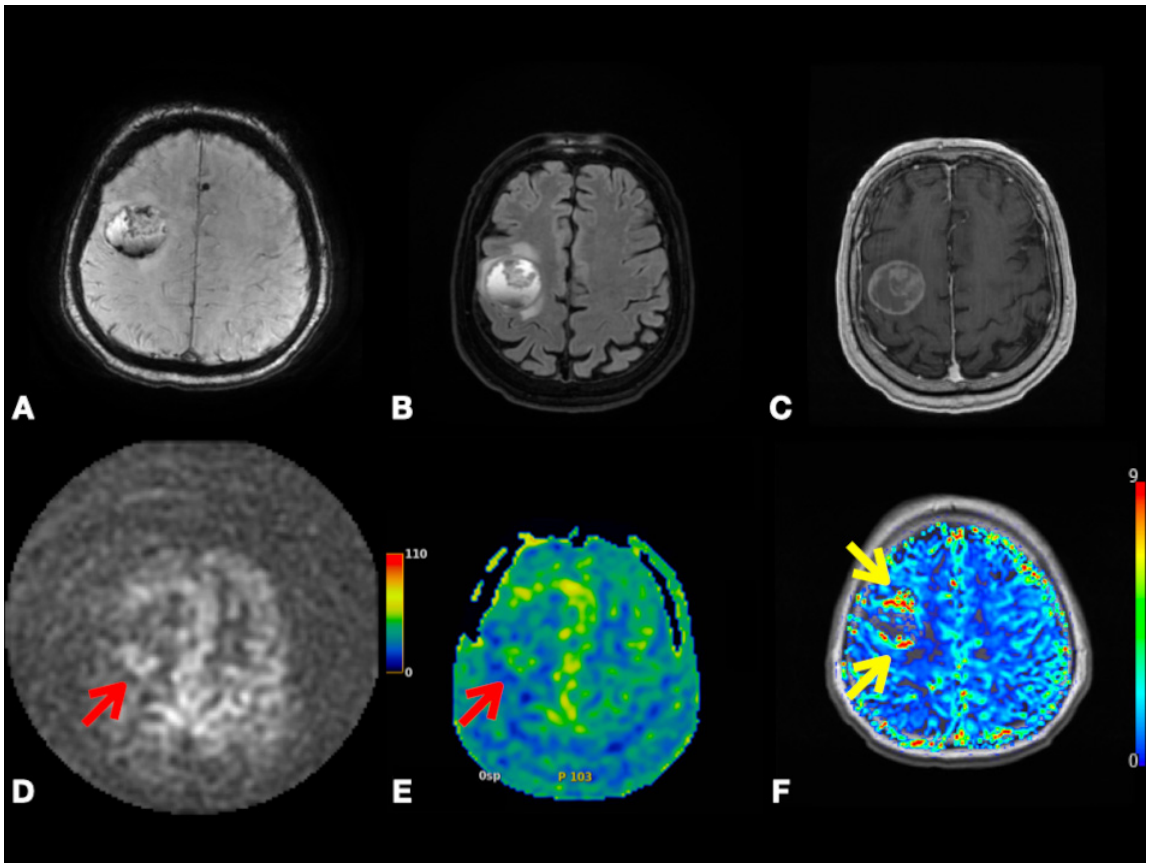

Fig. 8. Right frontal lobe non-small cell lung cancer metastasis. Axial SWI (A), FLAIR (B), and post-contrast T1-weighted (C) images depicting lesion with heterogenous enhancement, perilesional vasogenic edema, central necrosis, and intralesional hemorrhage. Axial pcASL source data (D), color-coded CBF map (E) from pcASL data, and color-coded rCBV map (F) from DSC data depicting heterogenous hyperperfusion amongst nodules at super lesion margin (red arrowheads) and enhancing margins elsewhere (yellow arrowheads). Abbreviations: SWI, Susceptibility weighted imaging; FLAIR, Fluid attenuated inversion recovery; pcASL, Pseudo-Continuous Arterial Spin Labeling; CBF, cerebral blood flow; rCBV, relative cerebral blood volume; DSC, Dynamic susceptibility contrast MR imaging.

ferentiate between them [144]. Presence of multiple lesions, location at grey-white junction, and vasogenic edema favor metastases or infection over primary brain tumors. Additionally, large tumor size with disproportionately little vasogenic edema and mass effect favor a primary brain tumor over metastases. However, on conventional MRI, both GBM and MTs are sometimes similar and may show heterogenous appearance with ring enhancement surrounded by edema [144,145]. As they have different management plans, accurate differentiation between GBM and MTs is mandatory.

On DSC, Calli *et al.* [146] found that maximum rCBV ratio is not statistically significant between GBM and MT. On DCE, Lu *et al.* [117] found that K_{trans} and V_e differences are not statistically significant to differentiate between GBM and MT. Similarly, another study demonstrated that there is no significant difference in K_{trans} and V_p between gliomas and MTs [147]. Using both DSC and DCE, Bauer *et al.* [148] found that the difference in both rCBV and K_{trans} is not statistically significant between gliomas and MTs. Using ASL, Sunwoo *et al.* [14] found that both tumoral and peritumoral normalized CBF and normalized CBV were significantly higher in the GBM group compared to the MT group. In contrast to tumoral DSC and DCE parameters that show a non-significant difference, another study found that peritumoral rCBV is significantly higher in glioma compared to MTs [149]. Additionally, peritumoral CBF is found to be statistically significant between GBM and MTs [115].

In Fig. 8, we present a case of right frontal lobe non-small cell lung cancer MT. Color-coded CBF map from pcASL data and color-coded rCBV map from DSC data show heterogenous hyperperfusion amongst nodules at super lesion margin and enhancing margins elsewhere. This demonstrates that MTs may show hyperperfusion using ASL or DSC. This highlights the importance of using quantitative parameters, such as tumoral and peritumoral CBV and CBF to compare between GBM and MTs as depending on observing hyperperfusion signals on the color-coded maps is subjective and can be misleading.

Table 3. Characteristics of studies included in our review of differentiating between glioma, lymphoma, and metastases (MTs) using dynamic contrast-enhanced (DCE), dynamic-susceptibility contrast (DSC), arterial spin labeling (ASL) and diffusion-weighted (DWI) MRI techniques.

Re.	Year	Study design	Number of patients	Age	M/F	Histopathology	Type of technique	Significant parameters
[104]	2002	R	37	N/A	N/A	HGG (21), LGG (8), LM (8)	DSC	rCBV ratio
[105]	2019	R	145	M = 53.3 Ra = 28–86	75/70	GBM (89), LM (56)	DSC	nCBV
[106]	2011	R	67	N/A	24/33	GBM (26), MT (25), LM (16)	DSC	rCBV
[107]	2014	R	60	M = 54 Ra = 25.0–83.0	33/27	GBM (41), LM (19)	DSC, DWI	Maximum nCBV, and minimum ADC
[108]	2014	R	38	N/A	21/17	HGG (26), LM (12)	DSC	rCBV
[109]	2010	R	62	M = 46 Ra = 15–73	33/29	GBM (28), MT (22), LM (12)	DSC	nCBV
[110]	2003	N/A	24	N/A	N/A	GBM (12), LM (12)	DSC	rrCBV ratio
[111]	2009	R	20	Ra = 14–72	13/7	HGG (11), LM (9)	DSC	maximum rCBV ratio
[112]	2015	R	28	N/A	13/15	GBM (18), LM (10)	DSC	cCBV ratio
[113]	2013	R	35	N/A	27/8	GBM (20), LM (15)	DSC	CBV ratio, cCBV ratio
[114]	2018	R	22	mean = 59.8 Ra = 7–86	11/11	HGG (14), LM (8)	DSC, DCE	cCBV, K_{trans}
[115]	2006	P	79	57 ± 14	43/36	HHG, LGG, MT, LM	DSC	CBF, Peritumoral CBF
[116]	2014	R	71	N/A	N/A	GBM (60), LM (11)	DCE	Median K_{ep} and Median K_{trans}
[117]	2016	R	75	N/A	40/35	GBM (38), LM (16), MT (21)	DCE	Mean K_{trans}, V_e
[118]	2019	P	35	N/A	20/15	HGG (21), LM (8), MT (6)	DSC, DCE	rCBF, V_e, K_{trans}
[149]	2004	P	26	25–76	12/14	HGG (14), LM (12)	DWI, DSC	Peritumoral rCBV, peritumoral ADC
[14]	2016	R	128	19–84	76/52	GBM (89)/MT (39)	ASL	nCBV, nCBF

Re., reference; R, retrospective; P, prospective; M, male; F, female; N/A, not applicable; GBM, glioblastoma; LM, lymphoma; MT, metastases; HGG, high grade glioma; LGG, low grade glioma; DSC, dynamic susceptibility contrast MRI; DWI, diffusion-weighted MRI; nCBV, normalized cerebral blood volume; nCBF, normalized cerebral blood flow; rCBV, relative cerebral blood volume; rrCBV, regional relative cerebral blood volume; cCBV, corrected cerebral blood volume; DCE, dynamic contrast-enhanced; V_e, extravascular extracellular volume per unit tissue volume; K_{trans}, volume transfer constant from plasma to extravascular extracellular space; K_{ep}, rate constant from extravascular extracellular space to plasma; ADC, apparent diffusion coefficient; ASL, arterial spin labeling MRI.

Using DWI, both tumoral and peritumoral ADC are found to be significantly higher in MTs compared to gliomas [149]. This finding suggests that MTs cause more edema and fluid production compared to gliomas [150]. The higher degree of edema in MTs can be explained by the differences in the BBB characteristics between gliomas and MTs. MTs completely lack a BBB and subsequently, cause prominent capillary fenestrations, while the BBB disruption in GBM varies and as a result, the degree of permeability can vary from normal to increased [151,152]. This can explain why ADC values are found to be higher in MTs. This increased fluid production and edema produced by MTs can also cause more compression on the microcirculation [153]. Eventually, the peritumoral rCBV decreases. This explains why rCBV is lower in MTs compared to gliomas. Table 3 (Ref. [14,104–118,149]) shows a summary of studies differentiating between glioma, lymphoma, and MTs using DCE, DSC, ASL, and DWI.

6. Conclusions

Advanced MRI techniques, such as DCE, DWI, ASL, DSC, and BOLD show promising methods to differentiate between various tumors and lesions that conventional MRI cannot define by comparing their physiologic characteristics, such as vascularity, permeability, oxygenation, and metabolism. Hopefully, these imaging modalities will help avoid invasive procedures, such as biopsy or traditional surgeries. More clinical studies with larger sample sizes should be encouraged to assess the significance of each advanced MRI technique and the specificity and sensitivity of each radiologic parameter.

Abbreviations

CNS, Central Nervous System; FMRI, Functional MR Imaging; DCE, Dynamic Contrast-Enhanced MR Imaging; DSC, Dynamic Susceptibility Contrast MR Imaging; DWI, Diffusion-Weighted Imaging; ASL, Arterial Spin Labeling MR Imaging; BOLD, Blood Oxygen Level-Dependent MR Imaging; CBF, Cerebral Blood Flow; CBV, Cerebral Blood Volume; MTT, Mean Transient Time; rCBV, Relative Cerebral Blood Volume; V_p, Fractional Plasma Volume; V_e, Fractional Volume of Extracellular Space Per Unit Tissue Volume; EES, Extracellular Space; K_{ep}, Efflux Rate Constant; SER, Maximum Signal-Enhancement Ratio; AUC, Area Under the Curve; GRASP, Golden-Angle Radial Sparse Parallel MR Imaging; CVR, Cerebrovascular Reactivity; TIC, Time-Intensity Curve; ADC, Apparent Diffusion Coefficient; SI, Signal Intensity; CVR, Cerebrovascular Reactivity; PG, Paraganglioma; SC, Schwannoma; MG, Meningioma; NF2, Neurofibromatosis type 2; PCNSL, Primary Central Nervous System Lymphoma; GBM, Glioblastoma Multiform; MT, Metastasis.

Author Contributions

AME took the responsibility for conceptualization, designing the study, and interpreting the data. AME prepared the figures. RTB prepared radiological figures and their descriptions. RWT, DMA, and HH provided help and advice on presenting the data. AME wrote the initial draft. RWT, DMA, and HH participated in writing the final draft. HH provided supervision and advice. All authors contributed to editorial changes in the manuscript. All authors read and approved the final manuscript. All authors have participated sufficiently in the work and agreed to be accountable for all aspects of the work.

Ethics Approval and Consent to Participate

Not applicable.

Acknowledgment

Not applicable.

Funding

This research received no external funding.

Conflict of Interest

The authors declare no conflict of interest.

References

[1] Louis DN, Perry A, Wesseling P, Brat DJ, Cree IA, Figarella-Branger D, *et al*. The 2021 WHO Classification of Tumors of the Central Nervous System: a summary. Neuro-Oncology. 2021; 23: 1231–1251.

[2] Singh S, Kumar A, Mehrotra A, Rao RN, Behari S. Nonsecretory Paraganglioma in Cavernous Sinus Masquerading as Meningioma. World Neurosurgery. 2019; 126: 399–404.

[3] Elsayed MA, Ibrahim AM, El Darawany MA, Ellabban MA. A Huge Carotid Space Schwannoma Arising from The Cervical Sympathetic Chain - A Case Report. Annals of Maxillofacial Surgery. 2021; 11: 144–147.

[4] Kleijwegt MC, van der Mey AGL, Wiggers-deBruine FT, Malessy MJA, van Osch MJP. Perfusion magnetic resonance imaging provides additional information as compared to anatomical imaging for decision-making in vestibular schwannoma. European Journal of Radiology Open. 2016; 3: 127–133.

[5] Cashmore MT, McCann AJ, Wastling SJ, McGrath C, Thornton J, Hall MG. Clinical quantitative MRI and the need for metrology. The British Journal of Radiology. 2021; 94: 20201215.

[6] Ota Y, Liao E, Capizzano AA, Kurokawa R, Bapuraj JR, Syed F, *et al*. Diagnostic Role of Diffusion-Weighted and Dynamic Contrast-Enhanced Perfusion MR Imaging in Paragangliomas and Schwannomas in the Head and Neck. AJNR. American Journal of Neuroradiology. 2021; 42: 1839–1846.

[7] Park SB. Functional MR imaging in gynecologic malignancies: current status and future perspectives. Abdominal Radiology. 2016; 41: 2509–2523.

[8] Wakefield JC, Downey K, Kyriazi S, deSouza NM. New MR techniques in gynecologic cancer. AJR. American Journal of Roentgenology. 2013; 200: 249–260.

[9] Koyama T, Togashi K. Functional MR imaging of the female pelvis. Journal of Magnetic Resonance Imaging. 2007; 25: 1101–1112.

[10] Koretsky AP. Early development of arterial spin labeling to measure regional brain blood flow by MRI. NeuroImage. 2012; 62: 602–607.
[11] Knutsson L, Börjesson S, Larsson EM, Risberg J, Gustafson L, Passant U, *et al*. Absolute quantification of cerebral blood flow in normal volunteers: correlation between Xe-133 SPECT and dynamic susceptibility contrast MRI. Journal of Magnetic Resonance Imaging. 2007; 26: 913–920.
[12] Jiang J, Zhao L, Zhang Y, Zhang S, Yao Y, Qin Y, *et al*. Comparative analysis of arterial spin labeling and dynamic susceptibility contrast perfusion imaging for quantitative perfusion measurements of brain tumors. International Journal of Clinical and Experimental Pathology. 2014; 7: 2790–2799.
[13] Haga S, Morioka T, Kameda K, Takahara K, Amano T, Tomohara S, *et al*. Subtraction of arterial spin-labeling magnetic resonance perfusion images acquired at dual post-labeling delay: Potential for evaluating cerebral hyperperfusion syndrome following carotid endarterectomy. Journal of Clinical Neuroscience. 2019; 63: 77–83.
[14] Sunwoo L, Yun TJ, You SH, Yoo RE, Kang KM, Choi SH, *et al*. Differentiation of Glioblastoma from Brain Metastasis: Qualitative and Quantitative Analysis Using Arterial Spin Labeling MR Imaging. PLoS ONE. 2016; 11: e0166662.
[15] Calamante F. Perfusion MRI using dynamic-susceptibility contrast MRI: quantification issues in patient studies. Topics in Magnetic Resonance Imaging. 2010; 21: 75–85.
[16] Mangla R, Kolar B, Zhu T, Zhong J, Almast J, Ekholm S. Percentage signal recovery derived from MR dynamic susceptibility contrast imaging is useful to differentiate common enhancing malignant lesions of the brain. AJNR. American Journal of Neuroradiology. 2011; 32: 1004–1010.
[17] Hackländer T, Reichenbach JR, Mödder U. Comparison of cerebral blood volume measurements using the T1 and T2* methods in normal human brains and brain tumors. Journal of Computer Assisted Tomography. 1997; 21: 857–866.
[18] Rempp KA, Brix G, Wenz F, Becker CR, Gückel F, Lorenz WJ. Quantification of regional cerebral blood flow and volume with dynamic susceptibility contrast-enhanced MR imaging. Radiology. 1994; 193: 637–641.
[19] Calamante F, Thomas DL, Pell GS, Wiersma J, Turner R. Measuring cerebral blood flow using magnetic resonance imaging techniques. Journal of Cerebral Blood Flow and Metabolism. 1999; 19: 701–735.
[20] Engvall C, Ryding E, Wirestam R, Holtås S, Ljunggren K, Ohlsson T, *et al*. Human cerebral blood volume (CBV) measured by dynamic susceptibility contrast MRI and 99mTc-RBC SPECT. Journal of Neurosurgical Anesthesiology. 2008; 20: 41–44.
[21] Bedekar D, Jensen T, Schmainda KM. Standardization of relative cerebral blood volume (rCBV) image maps for ease of both inter- and intrapatient comparisons. Magnetic Resonance in Medicine. 2010; 64: 907–913.
[22] Zimny A, Sasiadek M. Contribution of perfusion-weighted magnetic resonance imaging in the differentiation of meningiomas and other extra-axial tumors: case reports and literature review. Journal of Neuro-Oncology. 2011; 103: 777–783.
[23] Gaddikeri S, Gaddikeri RS, Tailor T, Anzai Y. Dynamic Contrast-Enhanced MR Imaging in Head and Neck Cancer: Techniques and Clinical Applications. AJNR. American Journal of Neuroradiology. 2016; 37: 588–595.
[24] Jung SC, Yeom JA, Kim JH, Ryoo I, Kim SC, Shin H, *et al*. Glioma: Application of histogram analysis of pharmacokinetic parameters from T1-weighted dynamic contrast-enhanced MR imaging to tumor grading. AJNR. American Journal of Neuroradiology. 2014; 35: 1103–1110.
[25] Verma S, Turkbey B, Muradyan N, Rajesh A, Cornud F, Haider MA, *et al*. Overview of dynamic contrast-enhanced MRI in prostate cancer diagnosis and management. AJR. American Journal of Roentgenology. 2012; 198: 1277–1288.
[26] Tofts PS. Modeling tracer kinetics in dynamic Gd-DTPA MR imaging. Journal of Magnetic Resonance Imaging. 1997; 7: 91–101.
[27] Sala E, Rockall A, Rangarajan D, Kubik-Huch RA. The role of dynamic contrast-enhanced and diffusion weighted magnetic resonance imaging in the female pelvis. European Journal of Radiology. 2010; 76: 367–385.
[28] Jackson A, O'Connor JPB, Parker GJM, Jayson GC. Imaging tumor vascular heterogeneity and angiogenesis using dynamic contrast-enhanced magnetic resonance imaging. Clinical Cancer Research. 2007; 13: 3449–3459.
[29] Feng L, Grimm R, Block KT, Chandarana H, Kim S, Xu J, *et al*. Golden-angle radial sparse parallel MRI: combination of compressed sensing, parallel imaging, and golden-angle radial sampling for fast and flexible dynamic volumetric MRI. Magnetic Resonance in Medicine. 2014; 72: 707–717.
[30] Mogen JL, Block KT, Bansal NK, Patrie JT, Mukherjee S, Zan E, *et al*. Dynamic Contrast-Enhanced MRI to Differentiate Parotid Neoplasms Using Golden-Angle Radial Sparse Parallel Imaging. AJNR. American Journal of Neuroradiology. 2019; 40: 1029–1036.
[31] Heacock L, Gao Y, Heller SL, Melsaether AN, Babb JS, Block TK, *et al*. Comparison of conventional DCE-MRI and a novel golden-angle radial multicoil compressed sensing method for the evaluation of breast lesion conspicuity. Journal of Magnetic Resonance Imaging. 2017; 45: 1746–1752.
[32] Motoshima S, Irie H, Nakazono T, Kamura T, Kudo S. Diffusion-weighted MR imaging in gynecologic cancers. Journal of Gynecologic Oncology. 2011; 22: 275–287.
[33] Levy A, Medjhoul A, Caramella C, Zareski E, Berges O, Chargari C, *et al*. Interest of diffusion-weighted echo-planar MR imaging and apparent diffusion coefficient mapping in gynecological malignancies: a review. Journal of Magnetic Resonance Imaging. 2011; 33: 1020–1027.
[34] Norman KA, Polyn SM, Detre GJ, Haxby JV. Beyond mind-reading: multi-voxel pattern analysis of fMRI data. Trends in Cognitive Sciences. 2006; 10: 424–430.
[35] Ogawa S, Lee TM, Kay AR, Tank DW. Brain magnetic resonance imaging with contrast dependent on blood oxygenation. Proceedings of the National Academy of Sciences of the United States of America. 1990; 87: 9868–9872.
[36] Kim DI, Sui J, Rachakonda S, White T, Manoach DS, Clark VP, *et al*. Identification of imaging biomarkers in schizophrenia: a coefficient-constrained independent component analysis of the mind multi-site schizophrenia study. Neuroinformatics. 2010; 8: 213–229.
[37] Greicius MD, Srivastava G, Reiss AL, Menon V. Default-mode network activity distinguishes Alzheimer's disease from healthy aging: evidence from functional MRI. Proceedings of the National Academy of Sciences of the United States of America. 2004; 101: 4637–4642.
[38] Davis TL, Kwong KK, Weisskoff RM, Rosen BR. Calibrated functional MRI: mapping the dynamics of oxidative metabolism. Proceedings of the National Academy of Sciences of the United States of America. 1998; 95: 1834–1839.
[39] Buxton RB, Wong EC, Frank LR. Dynamics of blood flow and oxygenation changes during brain activation: the balloon model. Magnetic Resonance in Medicine. 1998; 39: 855–864.
[40] Glover GH. Overview of functional magnetic resonance imaging. Neurosurgery Clinics of North America. 2011; 22: 133–139, vii.
[41] Hou X, Liu P, Li Y, Jiang D, De Vis JB, Lin Z, *et al*. The association between BOLD-based cerebrovascular reactivity (CVR) and end-tidal CO_2 in healthy subjects. NeuroImage. 2020; 207:

116365.
[42] Kansal A, Lahiri A, Nishikawa H. Sympathetic paraganglioma presenting with Horner's syndrome in a child. Journal of Plastic, Reconstructive & Aesthetic Surgery. 2006; 59: 772–774.
[43] Dandpat SK, Rai SKR, Shah A, Goel N, Goel AH. Silent stellate ganglion paraganglioma masquerading as schwannoma: A surgical nightmare. Journal of Craniovertebral Junction & Spine. 2020; 11: 240–242.
[44] Rao AB, Koeller KK, Adair CF. From the archives of the AFIP. Paragangliomas of the head and neck: radiologic-pathologic correlation. Armed Forces Institute of Pathology. Radiographics. 1999; 19: 1605–1632.
[45] Moyer JS, Bradford CR. Sympathetic paraganglioma as an unusual cause of Horner's syndrome. Head & Neck. 2001; 23: 338–342.
[46] Birchler MT, Landau K, Went PT, Stoeckli SJ. Paraganglioma of the cervical sympathetic trunk. The Annals of Otology, Rhinology, and Laryngology. 2002; 111: 1087–1091.
[47] van Baars FM, Cremers CW, van den Broek P, Veldman JE. Familiar non-chromaffinic paragangliomas (glomus tumors). Clinical and genetic aspects (abridged). Acta Oto-Laryngologica. 1981; 91: 589–593.
[48] Olsen WL, Dillon WP, Kelly WM, Norman D, Brant-Zawadzki M, Newton TH. MR imaging of paragangliomas. AJR. American Journal of Roentgenology. 1987; 148: 201–204.
[49] Wiemels J, Wrensch M, Claus EB. Epidemiology and etiology of meningioma. Journal of Neuro-oncology. 2010; 99: 307–314.
[50] Drevelegas A. Extra-axial brain tumors. European Radiology. 2005; 15: 453–467.
[51] Buetow MP, Buetow PC, Smirniotopoulos JG. Typical, atypical, and misleading features in meningioma. Radiographics. 1991; 11: 1087–1106.
[52] Amirjamshidi A, Mehrazin M, Abbassioun K. Meningiomas of the central nervous system occurring below the age of 17: report of 24 cases not associated with neurofibromatosis and review of literature. Child's Nervous System. 2000; 16: 406–416.
[53] Yamashita J, Handa H, Iwaki K, Abe M. Recurrence of intracranial meningiomas, with special reference to radiotherapy. Surgical Neurology. 1980; 14: 33–40.
[54] Watts J, Box G, Galvin A, Brotchie P, Trost N, Sutherland T. Magnetic resonance imaging of meningiomas: a pictorial review. Insights into Imaging. 2014; 5: 113–122.
[55] Komiyama M, Yagura H, Baba M, Yasui T, Hakuba A, Nishimura S, *et al*. MR imaging: possibility of tissue characterization of brain tumors using T1 and T2 values. AJNR. American Journal of Neuroradiology. 1987; 8: 65–70.
[56] Kutcher TJ, Brown DC, Maurer PK, Ghaed VN. Dural tail adjacent to acoustic neuroma: MR features. Journal of Computer Assisted Tomography. 1991; 15: 669–670.
[57] Wilms G, Lammens M, Marchal G, Demaerel P, Verplancke J, Van Calenbergh F, *et al*. Prominent dural enhancement adjacent to nonmeningiomatous malignant lesions on contrast-enhanced MR images. AJNR. American Journal of Neuroradiology. 1991; 12: 761–764.
[58] Senegor M. Prominent meningeal "tail sign" in a patient with a metastatic tumor. Neurosurgery. 1991; 29: 294–296.
[59] Tien RD, Yang PJ, Chu PK. "Dural tail sign": a specific MR sign for meningioma? Journal of Computer Assisted Tomography. 1991; 15: 64–66.
[60] Vogl TJ, Bisdas S. Differential diagnosis of jugular foramen lesions. Skull Base. 2009; 19: 3–16.
[61] Ong CK, Fook-Hin Chong V. Imaging of jugular foramen. Neuroimaging Clinics of North America. 2009; 19: 469–482.
[62] Arya S, Rao V, Juvekar S, Dcruz AK. Carotid body tumors: objective criteria to predict the Shamblin group on MR imaging. AJNR. American Journal of Neuroradiology. 2008; 29: 1349–1354.
[63] Radojkovic M, Mihailovic D, Stojanovic M, Radojković D. Large retroperitoneal schwannoma: a rare cause of chronic back pain. The Journal of International Medical Research. 2018; 46: 3404–3410.
[64] Ohba S, Miwa T, Kawase T. Trochlear nerve schwannoma with intratumoral hemorrhage: case report. Neurosurgery. 2006; 58: E791; discussion E791.
[65] Junaid M, Bukhari SS, Rashid MU. Optic nerve Schwannoma: Neurofibromatosus Type-1? A case report. The Journal of the Pakistan Medical Association. 2018; 68: 950–952.
[66] Crist J, Hodge JR, Frick M, Leung FP, Hsu E, Gi MT, *et al*. Magnetic Resonance Imaging Appearance of Schwannomas from Head to Toe: A Pictorial Review. Journal of Clinical Imaging Science. 2017; 7: 38.
[67] Tali ET, Yuh WT, Nguyen HD, Feng G, Koci TM, Jinkins JR, *et al*. Cystic acoustic schwannomas: MR characteristics. AJNR. American Journal of Neuroradiology. 1993; 14: 1241–1247.
[68] Lo PA, Harper CG, Besser M. Intracavernous schwannoma of the abducens nerve: a review of the clinical features, radiology and pathology of an unusual case. Journal of Clinical Neuroscience. 2001; 8: 357–360.
[69] Mulkens TH, Parizel PM, Martin JJ, Degryse HR, Van de Heyning PH, Forton GE, *et al*. Acoustic schwannoma: MR findings in 84 tumors. AJR. American Journal of Roentgenology. 1993; 160: 395–398.
[70] Hua Q, Xu Z, Jiang Y. Diagnosis and surgical treatment of carotid body tumor: A retrospective analysis of 58 patients. Oncology Letters. 2017; 14: 3628–3632.
[71] Wieneke JA, Smith A. Paraganglioma: carotid body tumor. Head and Neck Pathology. 2009; 3: 303–306.
[72] Ota Y, Liao E, Capizzano AA, Baba A, Kurokawa R, Kurokawa M, *et al*. Intracranial paragangliomas versus schwannomas: Role of dynamic susceptibility contrast perfusion and diffusion MRI. Journal of Neuroimaging. 2022; 32: 875–883.
[73] Malla SR, Bhalla AS, Manchanda S, Kandasamy D, Kumar R, Agarwal S, *et al*. Dynamic contrast-enhanced magnetic resonance imaging for differentiating head and neck paraganglioma and schwannoma. Head & Neck. 2021; 43: 2611–2622.
[74] Ota Y, Liao E, Capizzano AA, Yokota H, Baba A, Kurokawa R, *et al*. MR diffusion and dynamic-contrast enhanced imaging to distinguish meningioma, paraganglioma, and schwannoma in the cerebellopontine angle and jugular foramen. Journal of Neuroimaging. 2022; 32: 502–510.
[75] Pires A, Nayak G, Zan E, Hagiwara M, Gonen O, Fatterpekar G. Differentiation of Jugular Foramen Paragangliomas versus Schwannomas Using Golden-Angle Radial Sparse Parallel Dynamic Contrast-Enhanced MRI. AJNR. American Journal of Neuroradiology. 2021; 42: 1847–1852.
[76] Demerath T, Blackham K, Anastasopoulos C, Block KT, Stieltjes B, Schubert T. Golden-Angle Radial Sparse Parallel (GRASP) MRI differentiates head & neck paragangliomas from schwannomas. Magnetic Resonance Imaging. 2020; 70: 73–80.
[77] Lee KY, Oh YW, Noh HJ, Lee YJ, Yong HS, Kang EY, *et al*. Extraadrenal paragangliomas of the body: imaging features. AJR. American Journal of Roentgenology. 2006; 187: 492–504.
[78] Papiez J, Rojiani MV, Rojiani AM. Vascular alterations in schwannoma. International Journal of Clinical and Experimental Pathology. 2014; 7: 4032–4038.
[79] Skolnik AD, Loevner LA, Sampathu DM, Newman JG, Lee JY, Bagley LJ, *et al*. Cranial Nerve Schwannomas: Diagnostic Imaging Approach. Radiographics. 2016; 36: 1463–1477.
[80] Goldblum JR, Folpe AL, Weiss SW, Enzinger FM, Weiss SW. Enzinger and Weiss's Soft Tissue Tumors. 6th edn. Saunders/Elsevier: Philadelphia, PA, USA. 2014.
[81] Mehrotra N, Behari S, Pal L, Banerji D, Sahu RN, Jain VK. Giant

vestibular schwannomas: focusing on the differences between the solid and the cystic variants. British Journal of Neurosurgery. 2008; 22: 550–556.
[82] Asthagiri AR, Parry DM, Butman JA, Kim HJ, Tsilou ET, Zhuang Z, *et al*. Neurofibromatosis type 2. Lancet. 2009; 373: 1974–1986.
[83] Patronas NJ, Courcoutsakis N, Bromley CM, Katzman GL, MacCollin M, Parry DM. Intramedullary and spinal canal tumors in patients with neurofibromatosis 2: MR imaging findings and correlation with genotype. Radiology. 2001; 218: 434–442.
[84] Evans DGR, Moran A, King A, Saeed S, Gurusinghe N, Ramsden R. Incidence of vestibular schwannoma and neurofibromatosis 2 in the North West of England over a 10-year period: higher incidence than previously thought. Otology & Neurotology. 2005; 26: 93–97.
[85] Evans DGR. Neurofibromatosis type 2 (NF2): a clinical and molecular review. Orphanet Journal of Rare Diseases. 2009; 4: 16.
[86] Goutagny S, Kalamarides M. Meningiomas and neurofibromatosis. Journal of Neuro-Oncology. 2010; 99: 341–347.
[87] Evans DGR, Baser ME, O'Reilly B, Rowe J, Gleeson M, Saeed S, *et al*. Management of the patient and family with neurofibromatosis 2: a consensus conference statement. British Journal of Neurosurgery. 2005; 19: 5–12.
[88] Ota Y, Liao E, Capizzano AA, Baba A, Kurokawa R, Kurokawa M, *et al*. Neurofibromatosis type 2 versus sporadic vestibular schwannoma: The utility of MR diffusion and dynamic contrast-enhanced imaging. Journal of Neuroimaging. 2022; 32: 554–560.
[89] Gugel I, Zipfel J, Hartjen P, Kluwe L, Tatagiba M, Mautner VF, *et al*. Managing NF2-associated vestibular schwannomas in children and young adults: review of an institutional series regarding effects of surgery and bevacizumab on growth rates, tumor volume, and hearing quality. Child's Nervous System. 2020; 36: 2471–2480.
[90] Lewis D, Roncaroli F, Agushi E, Mosses D, Williams R, Li KL, *et al*. Inflammation and vascular permeability correlate with growth in sporadic vestibular schwannoma. Neuro-Oncology. 2019; 21: 314–325.
[91] Sobel RA, Wang Y. Vestibular (acoustic) schwannomas: histologic features in neurofibromatosis 2 and in unilateral cases. Journal of Neuropathology and Experimental Neurology. 1993; 52: 106–113.
[92] Hilton DA, Hanemann CO. Schwannomas and their pathogenesis. Brain Pathology. 2014; 24: 205–220.
[93] Sykopetrites V, Piras G, Taibah A, Sanna M. Meningiomas of the Internal Auditory Canal. The Laryngoscope. 2021; 131: E413–E419.
[94] Pavlisa G, Rados M, Pazanin L, Padovan RS, Ozretic D, Pavlisa G. Characteristics of typical and atypical meningiomas on ADC maps with respect to schwannomas. Clinical Imaging. 2008; 32: 22–27.
[95] Eraky AM, Keles A, Goodman SL, Baskaya MK. Serum long non-coding RNAs as potential noninvasive biomarkers for glioblastoma diagnosis, prognosis, and chemoresistance. Journal of Integrative Neuroscience. 2022; 21: 111.
[96] Sinicrope K, Batchelor T. Primary Central Nervous System Lymphoma. Neurologic Clinics. 2018; 36: 517–532.
[97] Ostrom QT, Patil N, Cioffi G, Waite K, Kruchko C, Barnholtz-Sloan JS. CBTRUS Statistical Report: Primary Brain and Other Central Nervous System Tumors Diagnosed in the United States in 2013-2017. Neuro-Oncology. 2020; 22: iv1–iv96.
[98] DeAngelis LM, Yahalom J, Heinemann MH, Cirrincione C, Thaler HT, Krol G. Primary CNS lymphoma: combined treatment with chemotherapy and radiotherapy. Neurology. 1990; 40: 80–86.
[99] Bellinzona M, Roser F, Ostertag H, Gaab RM, Saini M. Surgical removal of primary central nervous system lymphomas (PCNSL) presenting as space occupying lesions: a series of 33 cases. European Journal of Surgical Oncology. 2005; 31: 100–105.
[100] Batchelor TT. Primary central nervous system lymphoma: A curable disease. Hematological Oncology. 2019; 37: 15–18.
[101] Glantz MJ, Cole BF, Recht L, Akerley W, Mills P, Saris S, *et al*. High-dose intravenous methotrexate for patients with nonleukemic leptomeningeal cancer: is intrathecal chemotherapy necessary? Journal of Clinical Oncology. 1998; 16: 1561–1567.
[102] Bühring U, Herrlinger U, Krings T, Thiex R, Weller M, Küker W. MRI features of primary central nervous system lymphomas at presentation. Neurology. 2001; 57: 393–396.
[103] Coulon A, Lafitte F, Hoang-Xuan K, Martin-Duverneuil N, Mokhtari K, Blustajn J, *et al*. Radiographic findings in 37 cases of primary CNS lymphoma in immunocompetent patients. European Radiology. 2002; 12: 329–340.
[104] Cho SK, Na DG, Ryoo JW, Roh HG, Moon CH, Byun HS, *et al*. Perfusion MR imaging: clinical utility for the differential diagnosis of various brain tumors. Korean Journal of Radiology. 2002; 3: 171–179.
[105] Lee JY, Bjørnerud A, Park JE, Lee BE, Kim JH, Kim HS. Permeability measurement using dynamic susceptibility contrast magnetic resonance imaging enhances differential diagnosis of primary central nervous system lymphoma from glioblastoma. European Radiology. 2019; 29: 5539–5548.
[106] Wang S, Kim S, Chawla S, Wolf RL, Knipp DE, Vossough A, *et al*. Differentiation between glioblastomas, solitary brain metastases, and primary cerebral lymphomas using diffusion tensor and dynamic susceptibility contrast-enhanced MR imaging. AJNR. American Journal of Neuroradiology. 2011; 32: 507–514.
[107] Suh CH, Kim HS, Lee SS, Kim N, Yoon HM, Choi CG, *et al*. Atypical imaging features of primary central nervous system lymphoma that mimics glioblastoma: utility of intravoxel incoherent motion MR imaging. Radiology. 2014; 272: 504–513.
[108] Xing Z, You RX, Li J, Liu Y, Cao DR. Differentiation of primary central nervous system lymphomas from high-grade gliomas by rCBV and percentage of signal intensity recovery derived from dynamic susceptibility-weighted contrast-enhanced perfusion MR imaging. Clinical Neuroradiology. 2014; 24: 329–336.
[109] Ma JH, Kim HS, Rim NJ, Kim SH, Cho KG. Differentiation among glioblastoma multiforme, solitary metastatic tumor, and lymphoma using whole-tumor histogram analysis of the normalized cerebral blood volume in enhancing and perienhancing lesions. AJNR. American Journal of Neuroradiology. 2010; 31: 1699–1706.
[110] Hartmann M, Heiland S, Harting I, Tronnier VM, Sommer C, Ludwig R, *et al*. Distinguishing of primary cerebral lymphoma from high-grade glioma with perfusion-weighted magnetic resonance imaging. Neuroscience Letters. 2003; 338: 119–122.
[111] Liao W, Liu Y, Wang X, Jiang X, Tang B, Fang J, *et al*. Differentiation of primary central nervous system lymphoma and high-grade glioma with dynamic susceptibility contrast-enhanced perfusion magnetic resonance imaging. Acta Radiologica. 2009; 50: 217–225.
[112] Nakajima S, Okada T, Yamamoto A, Kanagaki M, Fushimi Y, Okada T, *et al*. Primary central nervous system lymphoma and glioblastoma: differentiation using dynamic susceptibility-contrast perfusion-weighted imaging, diffusion-weighted imaging, and (18)F-fluorodeoxyglucose positron emission tomography. Clinical Imaging. 2015; 39: 390–395.
[113] Toh CH, Wei KC, Chang CN, Ng SH, Wong HF. Differentiation of primary central nervous system lymphomas and glioblastomas: comparisons of diagnostic performance of dynamic sus-

ceptibility contrast-enhanced perfusion MR imaging without and with contrast-leakage correction. AJNR. American Journal of Neuroradiology. 2013; 34: 1145–1149.

[114] Murayama K, Nishiyama Y, Hirose Y, Abe M, Ohyu S, Ninomiya A, *et al*. Differentiating between Central Nervous System Lymphoma and High-grade Glioma Using Dynamic Susceptibility Contrast and Dynamic Contrast-enhanced MR Imaging with Histogram Analysis. Magnetic Resonance in Medical Sciences. 2018; 17: 42–49.

[115] Weber MA, Zoubaa S, Schlieter M, Jüttler E, Huttner HB, Geletneky K, *et al*. Diagnostic performance of spectroscopic and perfusion MRI for distinction of brain tumors. Neurology. 2006; 66: 1899–1906.

[116] Kickingereder P, Sahm F, Wiestler B, Roethke M, Heiland S, Schlemmer HP, *et al*. Evaluation of microvascular permeability with dynamic contrast-enhanced MRI for the differentiation of primary CNS lymphoma and glioblastoma: radiologic-pathologic correlation. AJNR. American Journal of Neuroradiology. 2014; 35: 1503–1508.

[117] Lu S, Gao Q, Yu J, Li Y, Cao P, Shi H, *et al*. Utility of dynamic contrast-enhanced magnetic resonance imaging for differentiating glioblastoma, primary central nervous system lymphoma and brain metastatic tumor. European Journal of Radiology. 2016; 85: 1722–1727.

[118] Xi YB, Kang XW, Wang N, Liu TT, Zhu YQ, Cheng G, *et al*. Differentiation of primary central nervous system lymphoma from high-grade glioma and brain metastasis using arterial spin labeling and dynamic contrast-enhanced magnetic resonance imaging. European Journal of Radiology. 2019; 112: 59–64.

[119] Molnár PP, O'Neill BP, Scheithauer BW, Groothuis DR. The blood-brain barrier in primary CNS lymphomas: ultrastructural evidence of endothelial cell death. Neuro-Oncology. 1999; 1: 89–100.

[120] Koeller KK, Smirniotopoulos JG, Jones RV. Primary central nervous system lymphoma: radiologic-pathologic correlation. Radiographics. 1997; 17: 1497–1526.

[121] Aronen HJ, Gazit IE, Louis DN, Buchbinder BR, Pardo FS, Weisskoff RM, *et al*. Cerebral blood volume maps of gliomas: comparison with tumor grade and histologic findings. Radiology. 1994; 191: 41–51.

[122] Hourani R, Brant LJ, Rizk T, Weingart JD, Barker PB, Horská A. Can proton MR spectroscopic and perfusion imaging differentiate between neoplastic and nonneoplastic brain lesions in adults? AJNR. American Journal of Neuroradiology. 2008; 29: 366–372.

[123] Ning X, Zhao C, Wang C, Zhang D, Luo Q. Intracranial Demyelinating Pseudotumor: A Case Report and Review of the Literature. Turkish Neurosurgery. 2017; 27: 146–150.

[124] Cha S, Knopp EA, Johnson G, Wetzel SG, Litt AW, Zagzag D. Intracranial mass lesions: dynamic contrast-enhanced susceptibility-weighted echo-planar perfusion MR imaging. Radiology. 2002; 223: 11–29.

[125] Blasel S, Pfeilschifter W, Jansen V, Mueller K, Zanella F, Hattingen E. Metabolism and regional cerebral blood volume in autoimmune inflammatory demyelinating lesions mimicking malignant gliomas. Journal of Neurology. 2011; 258: 113–122.

[126] Hiremath SB, Muraleedharan A, Kumar S, Nagesh C, Kesavadas C, Abraham M, *et al*. Combining Diffusion Tensor Metrics and DSC Perfusion Imaging: Can It Improve the Diagnostic Accuracy in Differentiating Tumefactive Demyelination from High-Grade Glioma? AJNR. American Journal of Neuroradiology. 2017; 38: 685–690.

[127] Topkan E, Topuk S, Oymak E, Parlak C, Pehlivan B. Pseudoprogression in patients with glioblastoma multiforme after concurrent radiotherapy and temozolomide. American Journal of Clinical Oncology. 2012; 35: 284–289.

[128] de Wit MCY, de Bruin HG, Eijkenboom W, Sillevis Smitt PAE, van den Bent MJ. Immediate post-radiotherapy changes in malignant glioma can mimic tumor progression. Neurology. 2004; 63: 535–537.

[129] Chamberlain MC, Glantz MJ, Chalmers L, Van Horn A, Sloan AE. Early necrosis following concurrent Temodar and radiotherapy in patients with glioblastoma. Journal of Neuro-Oncology. 2007; 82: 81–83.

[130] Siu A, Wind JJ, Iorgulescu JB, Chan TA, Yamada Y, Sherman JH. Radiation necrosis following treatment of high grade glioma–a review of the literature and current understanding. Acta Neurochirurgica. 2012; 154: 191–201; discussion 201.

[131] Brandsma D, Stalpers L, Taal W, Sminia P, van den Bent MJ. Clinical features, mechanisms, and management of pseudoprogression in malignant gliomas. The Lancet. Oncology. 2008; 9: 453–461.

[132] Zikou A, Sioka C, Alexiou GA, Fotopoulos A, Voulgaris S, Argyropoulou MI. Radiation Necrosis, Pseudoprogression, Pseudoresponse, and Tumor Recurrence: Imaging Challenges for the Evaluation of Treated Gliomas. Contrast Media & Molecular Imaging. 2018; 2018: 6828396.

[133] Wang S, Martinez-Lage M, Sakai Y, Chawla S, Kim SG, Alonso-Basanta M, *et al*. Differentiating Tumor Progression from Pseudoprogression in Patients with Glioblastomas Using Diffusion Tensor Imaging and Dynamic Susceptibility Contrast MRI. AJNR. American Journal of Neuroradiology. 2016; 37: 28–36.

[134] Barajas RF, Jr, Chang JS, Segal MR, Parsa AT, McDermott MW, Berger MS, *et al*. Differentiation of recurrent glioblastoma multiforme from radiation necrosis after external beam radiation therapy with dynamic susceptibility-weighted contrast-enhanced perfusion MR imaging. Radiology. 2009; 253: 486–496.

[135] Kong DS, Kim ST, Kim EH, Lim DH, Kim WS, Suh YL, *et al*. Diagnostic dilemma of pseudoprogression in the treatment of newly diagnosed glioblastomas: the role of assessing relative cerebral blood flow volume and oxygen-6-methylguanine-DNA methyltransferase promoter methylation status. AJNR. American Journal of Neuroradiology. 2011; 32: 382–387.

[136] Manning P, Daghighi S, Rajaratnam MK, Parthiban S, Bahrami N, Dale AM, *et al*. Differentiation of progressive disease from pseudoprogression using 3D PCASL and DSC perfusion MRI in patients with glioblastoma. Journal of Neuro-Oncology. 2020; 147: 681–690.

[137] Muscas G, van Niftrik CHB, Sebök M, Della Puppa A, Seystahl K, Andratschke N, *et al*. Distinct Cerebrovascular Reactivity Patterns for Brain Radiation Necrosis. Cancers. 2021; 13: 1840.

[138] Pak RW, Hadjiabadi DH, Senarathna J, Agarwal S, Thakor NV, Pillai JJ, *et al*. Implications of neurovascular uncoupling in functional magnetic resonance imaging (fMRI) of brain tumors. Journal of Cerebral Blood Flow and Metabolism. 2017; 37: 3475–3487.

[139] Batchelor TT, Reardon DA, de Groot JF, Wick W, Weller M. Antiangiogenic therapy for glioblastoma: current status and future prospects. Clinical Cancer Research. 2014; 20: 5612–5619.

[140] Gerstner ER, Batchelor TT. Antiangiogenic therapy for glioblastoma. Cancer Journal. 2012; 18: 45–50.

[141] Barajas RF, Jr, Phillips JJ, Parvataneni R, Molinaro A, Essock-Burns E, Bourne G, *et al*. Regional variation in histopathologic features of tumor specimens from treatment-naive glioblastoma correlates with anatomic and physiologic MR Imaging. Neuro-Oncology. 2012; 14: 942–954.

[142] Agarwal S, Sair HI, Yahyavi-Firouz-Abadi N, Airan R, Pillai JJ. Neurovascular uncoupling in resting state fMRI demonstrated in patients with primary brain gliomas. Journal of Magnetic Resonance Imaging. 2016; 43: 620–626.

[143] Fierstra J, van Niftrik B, Piccirelli M, Burkhardt JK, Pangalu A, Kocian R, *et al*. Altered intraoperative cerebrovascular reactivity in brain areas of high-grade glioma recurrence. Magnetic Resonance Imaging. 2016; 34: 803–808.

[144] Han Y, Zhang L, Niu S, Chen S, Yang B, Chen H, *et al*. Differentiation Between Glioblastoma Multiforme and Metastasis From the Lungs and Other Sites Using Combined Clinical/Routine MRI Radiomics. Frontiers in Cell and Developmental Biology. 2021; 9: 710461.

[145] Thammaroj J, Wongwichit N, Boonrod A. Evaluation of Perienhancing Area in Differentiation between Glioblastoma and Solitary Brain Metastasis. Asian Pacific Journal of Cancer Prevention. 2020; 21: 2525–2530.

[146] Calli C, Kitis O, Yunten N, Yurtseven T, Islekel S, Akalin T. Perfusion and diffusion MR imaging in enhancing malignant cerebral tumors. European Journal of Radiology. 2006; 58: 394–403.

[147] Jung BC, Arevalo-Perez J, Lyo JK, Holodny AI, Karimi S, Young RJ, *et al*. Comparison of Glioblastomas and Brain Metastases using Dynamic Contrast-Enhanced Perfusion MRI. Journal of Neuroimaging. 2016; 26: 240–246.

[148] Bauer AH, Erly W, Moser FG, Maya M, Nael K. Differentiation of solitary brain metastasis from glioblastoma multiforme: a predictive multiparametric approach using combined MR diffusion and perfusion. Neuroradiology. 2015; 57: 697–703.

[149] Chiang IC, Kuo YT, Lu CY, Yeung KW, Lin WC, Sheu FO, *et al*. Distinction between high-grade gliomas and solitary metastases using peritumoral 3-T magnetic resonance spectroscopy, diffusion, and perfusion imagings. Neuroradiology. 2004; 46: 619–627.

[150] Steen RG. Edema and tumor perfusion: characterization by quantitative 1H MR imaging. AJR. American Journal of Roentgenology. 1992; 158: 259–264.

[151] Wesseling P, Ruiter DJ, Burger PC. Angiogenesis in brain tumors; pathobiological and clinical aspects. Journal of Neuro-Oncology. 1997; 32: 253–265.

[152] Jinnouchi T, Shibata S, Fukushima M, Mori K. Ultrastructure of capillary permeability in human brain tumor–Part 6: Metastatic brain tumor with brain edema. No Shinkei Geka. Neurological Surgery. 1988; 16: 563–568.

[153] Hossman KA, Blöink M. Blood flow and regulation of blood flow in experimental peritumoral edema. Stroke. 1981; 12: 211–217.